



A joint satellite and global cloud-resolving model analysis of a Madden-Julian Oscillation event: Model diagnosis

H. Masunaga,¹ M. Satoh,^{2,3} and H. Miura³

Received 9 February 2008; revised 13 May 2008; accepted 8 July 2008; published 12 September 2008.

[1] In this study, a methodology to diagnose a global cloud-resolving model (GCRM) is explored on the basis of a joint analysis with satellite measurements. The Madden-Julian Oscillation experiment carried out with the Nonhydrostatic Icosahedral Atmospheric Model (NICAM) is used as the test bed. The NICAM output is compared with Tropical Rainfall Measuring Mission (TRMM) and CloudSat measurements in terms of composite analysis, contoured frequency by altitude diagrams (CFADs), and the joint histogram of cloud top and precipitation top heights. It is found in the composite diagram that the GCRM reproduces a slow, eastward migration of a convective envelope well comparable to the satellite measurement. The GCRM CFAD qualitatively reproduces TRMM and CloudSat CFADs, except that the GCRM tends to overly produce snow in deep convection. The joint histograms reveal that, while the overproduction of snow is evident, NICAM-simulated snow is incapable of producing 94-GHz radar echoes higher than 5 dBZ. This deficiency can be mitigated by a modification to microphysical parameterization in the way that a proportion of small particles is enhanced in the snow mass spectrum.

Citation: Masunaga, H., M. Satoh, and H. Miura (2008), A joint satellite and global cloud-resolving model analysis of a Madden-Julian Oscillation event: Model diagnosis, *J. Geophys. Res.*, *113*, D17210, doi:10.1029/2008JD009986.

1. Introduction

[2] Efforts are underway to develop next-generation GCMs with less or no dependence on subgrid-scale parameterizations. Multiscale modeling framework (MMF) or superparameterization [Randall *et al.*, 2003] is among those efforts, where a two-dimensional cloud-resolving model (CRM) is embedded in each GCM grid box so that the computational burden required for the explicit treatment of cumulus-scale physics is reduced to a practical level. Another strategy aimed at next-generation GCMs is to directly expand the CRM coverage to the entire globe. A global CRM (GCRM) is an ultimate form to simulate cumulus convection across the whole planet. Although it is extremely demanding in computational cost, GCRM simulation is now feasible by use of cutting-edge supercomputers. Such recent progress in global atmospheric models with the explicit representation of convective clouds has invoked a need for new metrics to diagnose model-simulated clouds in comparison with satellite observations.

[3] Outgoing longwave radiation (OLR) and surface rain rate are widely used for interfacing simulated cloud and precipitation with observations. These parameters per se, however, are not necessarily optimal metrics. OLR does not differentiate deep convection from opaque cirrus, let alone make detailed soundings of in-cloud structure. Surface rain rate is not very informative either for profiling the nature of clouds aloft. An alternative observational tool more suitable for studying the cloud internal structure in depth is spaceborne radars. Satoh *et al.* [2008b] examined GCRM-simulated precipitation statistics together with Tropical Rainfall Measuring Mission (TRMM) Precipitation Radar (PR) observations. The statistics of vertical precipitation profiles analyzed by Satoh *et al.* [2008b] provides a compelling example demonstrating that a satellite radar is promising for evaluating GCRM simulations. Care must be taken, however, when using precipitation rate derived from satellite measurements because it largely depends on externally determined parameters, such as the Z-R relation coefficients, implemented in the retrieval algorithm. The built-in assumptions are a source of uncertainties which could introduce a nonnegligible statistical bias in the retrieved product [e.g., Berg *et al.*, 2006]. Precipitation rate, furthermore, is only remotely related to cloud microphysics, so that precipitation rate is generally not practical for the purpose of validating the microphysical model that may be critical for the CRM performance.

[4] These limitations may be circumvented by using directly observable parameters, instead of geophysical

¹Hydrospheric Atmospheric Research Center, Nagoya University, Nagoya, Japan.

²Center for Climate System Research, University of Tokyo, Tokyo, Japan.

³Frontier Research Center for Global Change, Japan Agency for Marine-Earth Science and Technology, Yokohama, Japan.

parameters such as precipitation rate, for the model evaluation. For example, observed radar reflectivity can be analyzed together with the synthesized radar reflectivity that is computed from simulated hydrometeor profiles and the associated meteorological variables. This approach, based on a forward radiative-transfer model, is unaffected by the additional uncertainties arising from an inversion model required for satellite retrieval algorithms. Another benefit of exploiting forward models is that microphysical parameterizations are testable by repeating multiple radiative-transfer calculations with different microphysical setups.

[5] The present paper explores a methodology to analyze the synthesized “observation” from GCRM outputs in conjunction with actual satellite measurements primarily from the TRMM PR and CloudSat Cloud Profiling Radar (CPR). The test bed simulation analyzed in this study is a recent GCRM experiment of an Madden-Julian Oscillation (MJO) event [Miura *et al.*, 2007]. The MJO has been one of the most appealing and challenging problems in tropical meteorology for decades since first documented by *Madden and Julian* [1971, 1972]. Observational and theoretical studies to date have vastly enriched our knowledge on the MJO, whereas further work has yet to be done for a better model reproducibility of the MJO. Model intercomparison studies [Slingo *et al.*, 1996; Lin *et al.*, 2006] revealed that a majority of general circulation models (GCMs) have difficulty in simulating the MJO with proper period and amplitude. A key problem arises partly (or mostly) from cumulus parameterizations, which limit the model capability to flexibly represent interactions between cumulus convection and large-scale dynamics. Compared to (typical) conventional GCMs, MMF simulations produce realistic eastward movement of convective envelope reminiscent of the MJO [Grabowski, 2003; Randall *et al.*, 2003]. Miura *et al.* [2007] and Inoue *et al.* [2008] demonstrated that their GCRM experiment yielded a migrating convective envelope and the accompanied cloud clusters remarkably similar to the observed MJO. The aforementioned studies suggest that the MJO offers an excellent benchmark to test the performance of global atmospheric models.

[6] The present work is focused on a methodology to identify potential model deficiencies by comparison with satellite measurements. The thorough evaluation of NICAM simulations is outside the scope of this paper. General issues concerning the current model setups such as the influence of coarse grid spacing are investigated in separate studies. The dependence on grid resolution was examined by Tomita *et al.* [2005] on the basis of a NICAM aqua-planet experiment. The dynamic and thermodynamic structure of eastward moving convective envelopes simulated with the NICAM was analyzed in detail by Nasuno *et al.* [2008] for the aqua-planet experiment and by Miura *et al.* [2007] and T. Nasuno *et al.* (Multi-scale organization of convection in a global numerical simulation of the December 2006 MJO event using explicit moist processes, submitted to *Journal of the Meteorological Society of Japan*, 2008) for the MJO experiment. Continuous efforts are being made to evaluate and improve the NICAM performance.

[7] The GCRM and satellite data sets employed in this work are described in section 2. The analysis results are

shown in section 3 and discussed in section 4. Conclusions are summarized in section 5.

2. Model and Data

2.1. Global Cloud-Resolving Model

[8] In this study, we further analyze the GCRM simulation of an MJO event conducted by Miura *et al.* [2007] with the Nonhydrostatic Icosahedral Atmospheric Model (NICAM) [Satoh *et al.*, 2008a]. The experiment spans a month from 15 December 2006 to 15 January 2007, which encompasses a major portion of an MJO episode. This particular MJO event hit Malaysia in the middle December of 2006, and caused a devastating flush flood. Three different numerical experiments were performed with different horizontal resolutions of about 14 km, 7 km, and 3.5 km, the last of which was applied to only a week-long period from 25 December 2006. The 7-km resolution run is adopted throughout the present study because it is considered to be better in accuracy than the 14-km run and longer in period than the 3.5-km experiment. Although the characteristics of individual cloud systems are affected by the choice of grid spacing, the general nature of convective response to a large-scale forcing is reasonably simulated for all grid resolutions tested with the NICAM [Tomita *et al.*, 2005; Miura *et al.*, 2007]. Simulated snapshots throughout the global tropics (20°S–20°N) are sampled at every 6 hour in this study.

[9] A forward radiative-transfer calculation is applied offline to the NICAM experiment for comparison with satellite measurements. The 14- and 94-GHz radar reflectivities are computed with gaseous and hydrometeor attenuations taken into account. The hydrometeor species considered in the radar measurement synthesis are rain, snow, cloud water, and cloud ice in accordance with the bulk microphysical model by Grabowski [1998], which is implemented in the NICAM MJO experiment. A simplified model of melting particles [Masunaga and Kummerow, 2005] is included as well so that the radar bright band is reproduced. The back-scattering and extinction coefficients are calculated for each hydrometeor species assuming the Mie approximation. The particle mass and size distribution of precipitating hydrometeors (rain and snow) assumed for the Mie calculation exactly follow the definition by Grabowski [1998] except where otherwise indicated. The dielectric constant for snow is computed by the Maxwell-Garnett model of ice matrix with air inclusions [Olson *et al.*, 2001]. The cloud size spectrum is approximated by a gamma distribution with a fixed mode radius for liquid droplets and by the Heymsfield and Platt [1984] parameterization for ice crystals.

2.2. Satellite Data

[10] The TRMM Level-1 PR reflectivity (1C21) and CloudSat Level-2 CPR reflectivity (2B-GEOPROF) data sets are used in this study. The TRMM PR is a 14-GHz radar with the horizontal resolution of 4.1 km at nadir and the vertical resolution of 250 m. The CloudSat CPR, operated at 94 GHz, has the spatial resolutions of 2 km (cross-track) and 1 km (along-track) horizontally and 500 m vertically. The minimum detectable echo is 19 dBZ for the TRMM PR (after the orbital boost in August 2001) and –28 dBZ for the CloudSat CPR. The difference in frequency

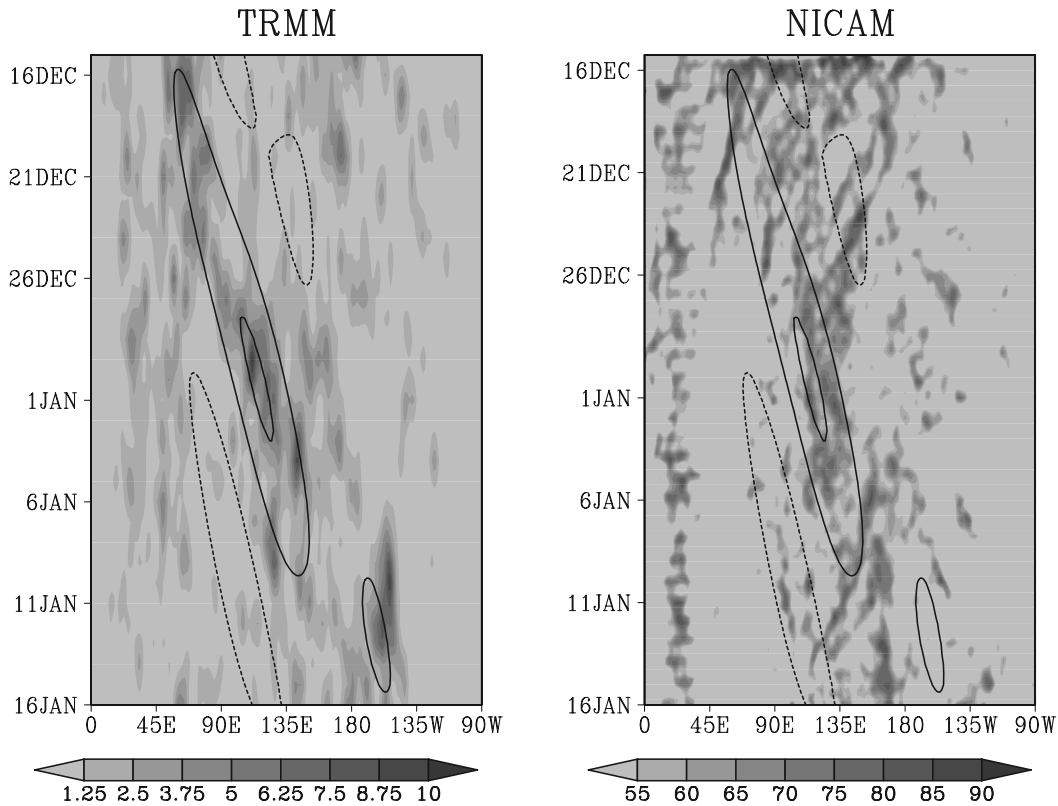


Figure 1. The time-longitude section of deep storm coverage (see text for definition) for (left) TRMM observation and (right) NICAM. The bandpass filtered MJO is contoured at every 2σ by solid (dashed) line for positive (negative) anomalies with zero contour omitted.

and sensitivity between the PR and CPR enables us to study different aspects of cloud and precipitation. The CloudSat CPR detects a broad range of hydrometeor species including nonprecipitating cloud droplets, drizzle, rain drops, and snow. Radar echoes from thick clouds and heavy precipitation, however, suffer from severe hydrometeor attenuation. The TRMM PR has a marginal sensitivity to snow and does not detect cloud droplets and ice crystals at all. The reflectivity profiles measured by the PR, on the other hand, are less attenuated than the CPR reflectivity. Infrared ($10.8 \mu\text{m}$) brightness temperature from the TRMM Visible/Infrared Scanner (VIRS) 1B01 product is also employed to supplement PR measurements following the manner proposed by Masunaga *et al.* [2005].

[11] Observation by low Earth orbiting (LEO) satellites is highly inhomogeneous in spatial and temporal sampling, restricted by satellite orbits and the scan geometry of sensors. No attempt, however, is made in the present study to sample the GCRM simulation according to the TRMM and CloudSat orbital swaths. Little benefit is expected from doing so, given that our interest lies not in the individual matching of a simulated cloud with an observed but in the overall statistics.

3. Analysis Results

3.1. Time-Longitude Section

[12] Examined first is the time-longitude section of deep storm coverage for observed and simulated clouds integrated meridionally between 20°S and 20°N . Deep storm coverage

is defined as the area fraction occupied by precipitating clouds with PR echo-top heights higher than 4 km and infrared brightness temperatures colder than 245 K. This definition is equivalent to the Deep Stratiform and Deep Convective categories combined together according to the terminology introduced by Masunaga *et al.* [2005]. The MJO is extracted by a space-time bandpass filter applied to the time-longitude section of TRMM deep storm coverage. The time period used for the bandpass filtering spans a whole year from April 2006 to March 2007. The MJO filter is bound by 20 and 80 days in period and 1 and 7 in zonal wave number [Masunaga *et al.*, 2006]. The time-longitude section of TRMM deep storm coverage is smoothed by multiple passes of the 1-2-1 filter, aimed at removing sampling noise in the TRMM observation. The identical smoothing is applied to the NICAM simulation as well, although not necessarily required for the high sampling rate of the model, in order to assure methodological consistency.

[13] The TRMM observation exhibits an eastward migration of convective envelope visually recognizable within the filtered MJO (Figure 1). The NICAM simulation starts with a broad convective area extending across the whole eastern hemisphere, which gradually settles down into a narrower convective band by 26 December. In the remainder of the period the convective envelope appears to closely follow the filtered MJO defined from the TRMM observation. Also successfully simulated by the NICAM is the embedded structure of cloud clusters moving to west [Nakazawa, 1988; Inoue *et al.*, 2008]. Diurnally modulated convective

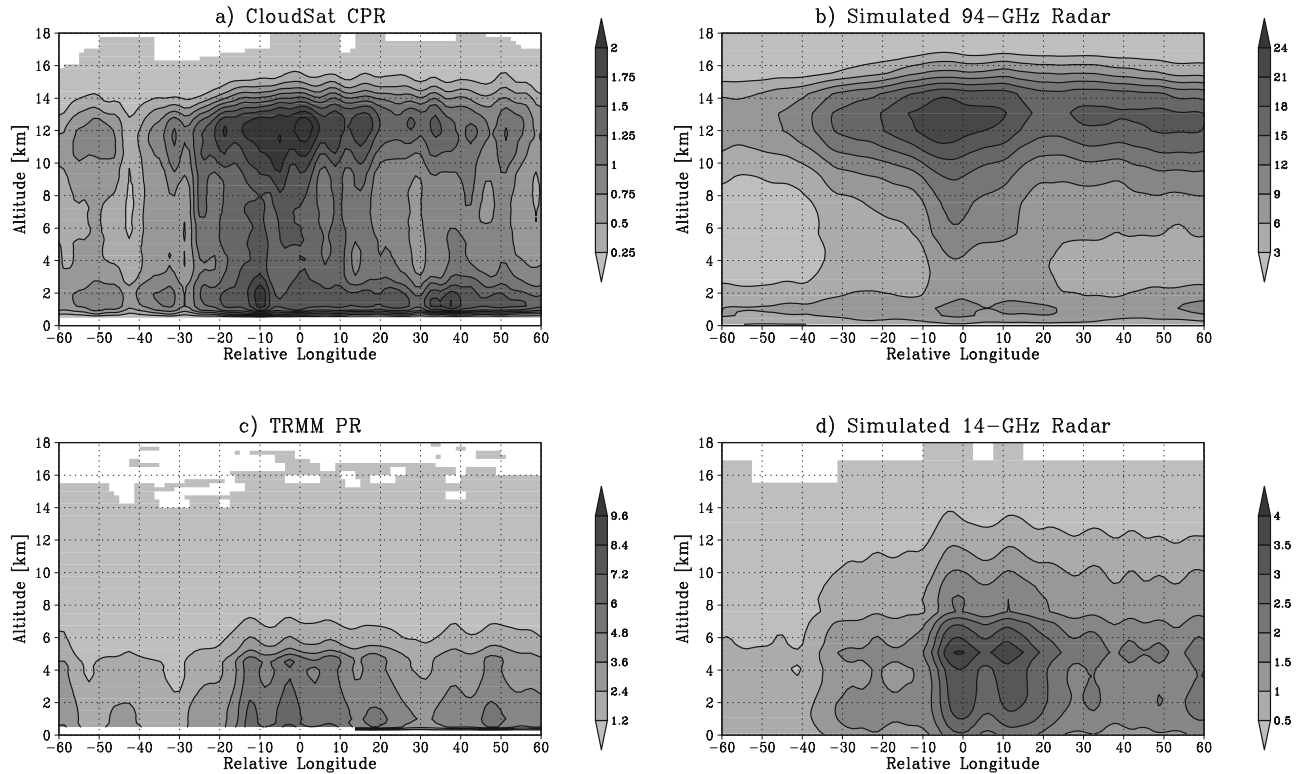


Figure 2. The number count of detected radar echo composited around the MJO convective peak for (a) CloudSat CPR, (b) NICAM synthesized 94-GHz reflectivity, (c) TRMM PR, and (d) NICAM synthesized 14-GHz reflectivity. The detectability limit is given as -28 dBZ for CPR/94-GHz and 19 dBZ for PR/14-GHz.

signals standing over Africa [e.g., *Yang and Slingo*, 2001] can be seen as a striped structure around 30°E . These high-frequency variabilities are absent in the TRMM observation, because of the low revisit frequency of TRMM satellite overpasses. A large inconsistency between the observation and model simulation, however, lies in the magnitude of deep storm coverage. Simulated clouds are larger in deep storm coverage than observed clouds by almost an order of magnitude. This bias results from the excessive production of snow in deep convective clouds simulated by the model as will be confirmed later.

3.2. Composite Analysis

[14] A composite analysis is performed with respect to a spatially movable base point defined along the MJO ridge in the time-longitude domain. The procedure is briefly discussed as follows (see *Masunaga et al.* [2006] for details). A time series of the local spatial maxima of the filtered MJO is first identified. The base point for the MJO wet phase is given by the local maxima that exceeds twice the standard deviation (2σ) of the filtered MJO anomaly. The local maxima that occurred in the east of the dateline from 10 to 15 January (see Figure 1) are not included in the analysis since this particular event appears not to be directly associated with the MJO episode of interest. The MJO dry phase is defined in the same manner but using the local minima of the filtered MJO.

[15] Figure 2 is the composite height-longitude structure of the MJO in terms of the number count of detected radar

echoes. The CloudSat CPR profile (Figure 2a) is double-peaked in altitude at 12 km and 1 – 2 km, implying the predominance of cirrus and shallow clouds. The zonal distribution of detected CPR echo is loosely peaked around 0° , or the MJO convective peak, and to its west. The cloud deck extending westward presumably corresponds to the stratiform anvil left behind the MJO convective peak [e.g., *Morita et al.*, 2006]. In the composite PR profile (Figure 2c), detected signals are confined in the lower half of the troposphere. The absence of radar echo above the freezing level, typically 4 – 5 km in height for tropical latitudes, is due to the PR insensitivity to frozen hydrometeors [*Masunaga et al.*, 2002]. A shallow-topped radar echo is observed at the leading edge of the MJO envelope or to the $\sim 20^{\circ}$ east of the MJO convective peak, while a thick precipitation layer reminiscent of stratiform anvil is extended to the west. Despite large contaminative noise, these composite features are consistent with existing knowledge on the MJO structure [*Lin and Johnson*, 1996; *Kiladis et al.*, 2005].

[16] The composited 94-GHz and 14-GHz radar profiles, for comparison with the Cloud CPR and TRMM PR, respectively, that are synthesized from the NICAM output are plotted in Figures 2b and 2d. It is found that radar echo detected above the freezing level is exaggerated compared to the observations. This indicates that frozen precipitating particles are excessively produced in the NICAM experiment. Nevertheless, the zonal amplitude modulation in the composite diagram is relatively well reproduced by the NICAM. Given the fact that the synthesized radar profiles

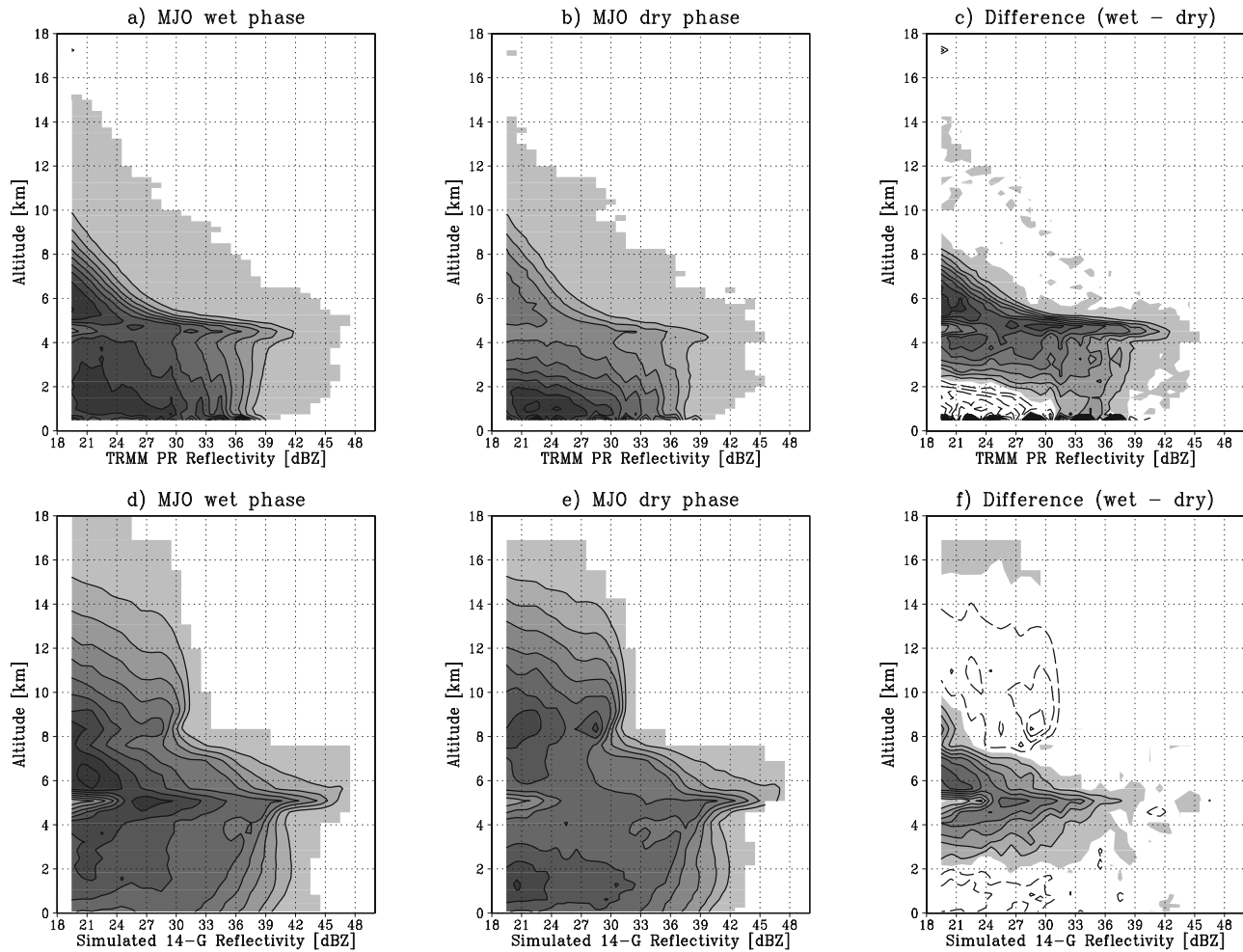


Figure 3. TRMM PR CFADs constructed for (a) the MJO wet phase, (b) dry phase, and (c) the difference between the two phases. (d–f) Same as Figures 3a–3c but constructed from the NICAM-synthesized 14-GHz radar reflectivity. Contour is linearly spaced in an arbitrary unit. Negative contours are dashed without shade in Figures 3c and 3f.

are composited with respect to the observed MJO convective peak, it would be fair to claim that the NICAM is reasonably successful in capturing the eastward migration of MJO convection.

3.3. Contoured Frequency by Altitude Diagram (CFAD)

[17] The vertical structure of cloud and precipitation varies systematically with zonal distance away from the MJO convective peak (Figure 2). The resultant contrast between the MJO wet (i.e., convectively active) phase and dry (inactive) phase may be used for a brief exercise to examine the model reproducibility of convective clouds associated with the MJO. To this end, the contoured frequency by altitude diagrams (CFADs), or the probability distribution of radar reflectivity at different altitudes, is constructed separately for different phases of the MJO. The MJO wet (dry) phase is defined as a domain where the filtered MJO anomaly is larger than 2σ (smaller than -2σ), which is indicated by the outermost solid (dashed) contour in Figure 1.

[18] Figure 3 shows the TRMM PR CFAD and the NICAM synthesized 14-GHz CFAD. The PR insensitivity to frozen hydrometeors is evident here again (Figures 3a and 3b) as implied by an abrupt drop in reflectivity above the freezing level. The freezing level is clearly highlighted by the radar bright band. The differential CFAD between the opposing MJO phases (Figure 3c) shows that the dry phase dominates the wet phase for altitudes lower than 2 km and reflectivities lower than 30 dBZ while the relationship reverses elsewhere. This dipolar structure confirms an increase of shallow cumulus population and a decrease of deep convection in the MJO dry phase. The differential CFAD constructed from the NICAM simulation, however, is tripolar (Figure 3f). An additional negative pole in the upper troposphere arises from a train of spurious convection initially prevailing across the eastern hemisphere (Figure 1) since this third pole almost disappears when the differential CFAD is reconstructed with the first 10 days removed (not shown). Synthesized CFAD pattern for individual MJO phases (Figures 3d and 3e) is spread out to higher altitudes and higher reflectivity than the observed CFAD. Overall,

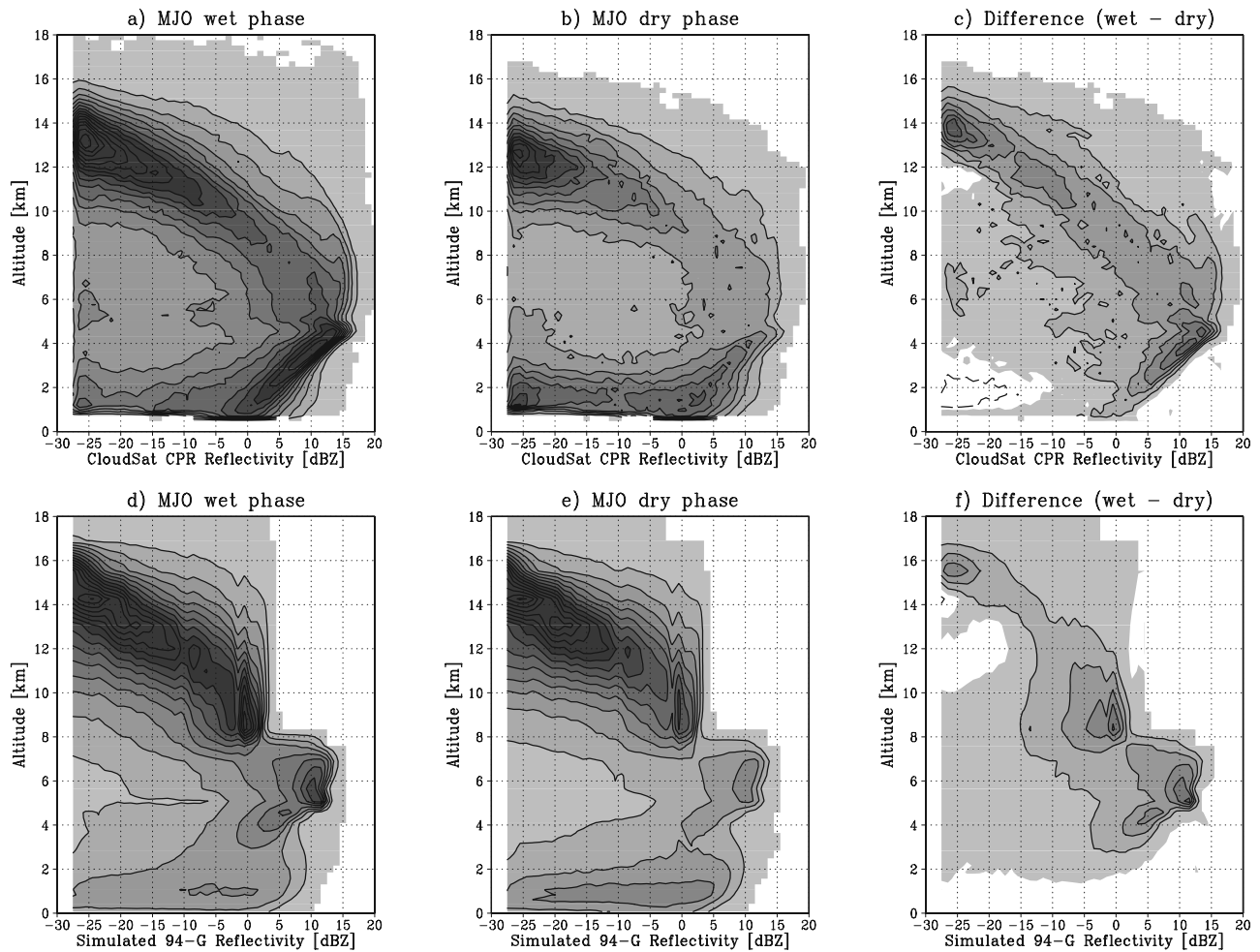


Figure 4. Same as Figure 3 but for the CloudSat CPR and the synthesized 94-GHz reflectivity.

tropical convection tends to be developed too deep in the NICAM simulation.

[19] Figure 4 shows CPR/94-GHz CFADs. The observed CFAD (Figures 4a–4c) is characterized by an arc-like structure that penetrates through the whole troposphere. Radar reflectivity increases with decreasing altitude along the upper branch of the arc, corresponding to the transition from cloud ice to precipitation ice (which potentially includes any of snow, graupel, and hail), until reflectivity achieves its maximum around 15 dBZ at the melting layer. Below the dBZ maximum, a jump in the water dielectric constant occurring from ice to liquid phases accentuates the lower branch of the arc in the MJO wet phase (Figure 4a). Strong rain attenuation makes radar reflectivity rapidly decline toward the ground. In the dry phase (Figure 4b) a majority of precipitation does not experience the cold rain processes, so that the discontinuity caused by melting is fainter. A reduced productivity of precipitation ice also accounts for the shrinkage of the upper branch in Figure 4b compared to Figure 4a. Cirrus clouds lingering near the tropopause, marked by the upper end of the arc, are present regardless of the MJO phases.

[20] A similar arc-like structure is present in the NICAM-synthesized CFAD (Figures 4d–4f), although the upper branch is exaggerated because of, as already seen, overly

produced snow in deep convective clouds. Interestingly, the synthesized 94-GHz radar echo appears to avoid entering a rectangular domain sharply edged at 5 dBZ and 8 km. This empty rectangle is obviously unrealistic, as no hint of such discontinuity is found in the observed CFAD. It turns out that the simulated properties of snow are to be questioned. The vertical distribution of individual hydrometeor species (Figure 5) shows that rain and cloud water are trapped below 8 km while cloud ice is isolated within a pair of separate layers near 6 km and the tropopause. Snow is the only candidate that can explain the continuous vertical rise extending above 8 km shown in Figures 4d–4f. In Figure 5, however, snow water content (or snow mixing ratio multiplied by dry air density) per se does not exhibit any apparent feature that explains the sharp CFAD cutoff. This issue will be discussed later in section 4.

3.4. Cloud and Precipitation Top Heights

[21] Masunaga *et al.* [2005] and Masunaga and Kummerow [2006] analyzed TRMM PR and VIRS measurements to investigate a broad spectrum of tropical precipitating clouds from shallow cumulus to deep convection. They used TRMM PR echo-top height and VIRS infrared brightness temperature as a proxy of precipitation top height (PTH) and cloud top height (CTH), respectively.

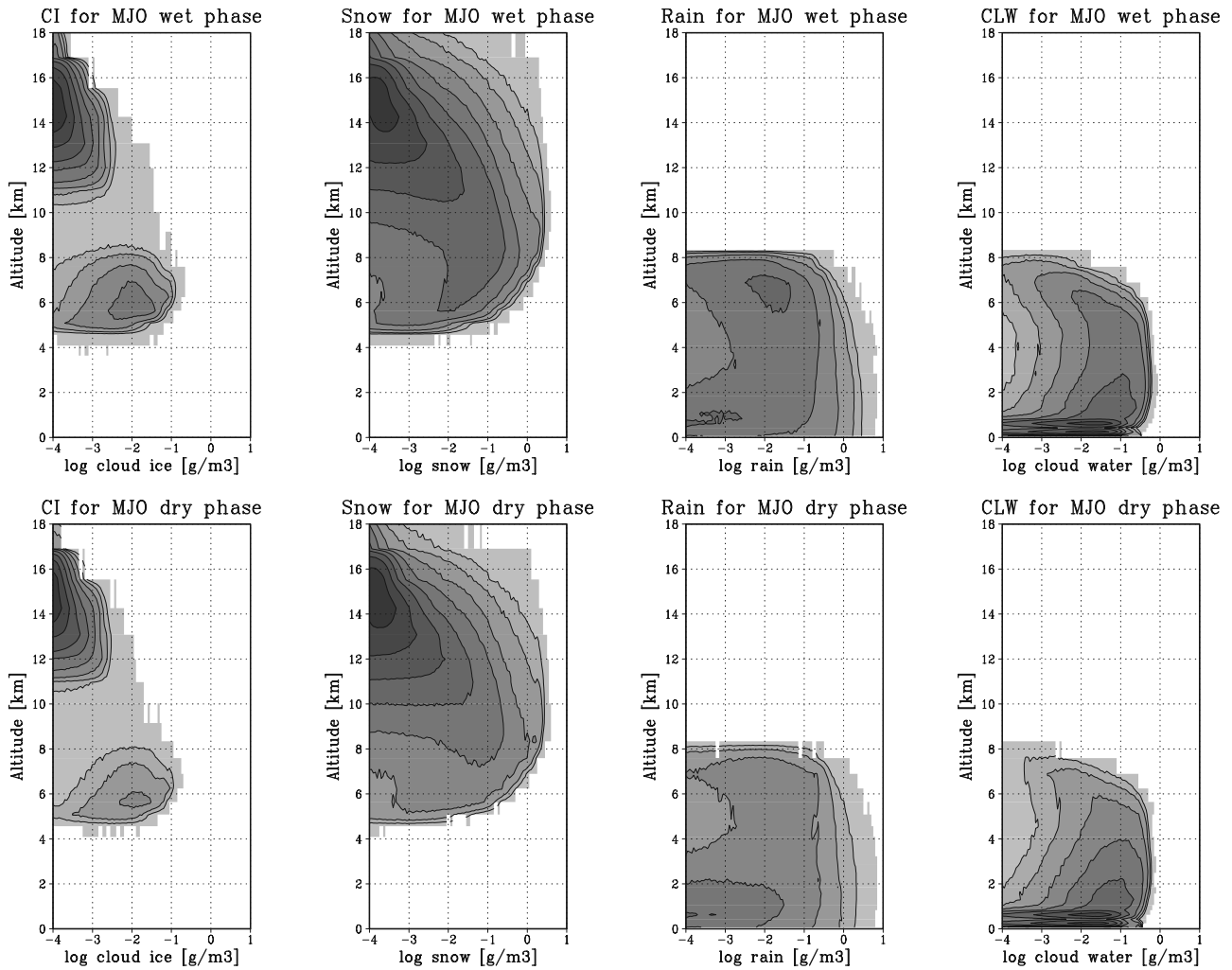


Figure 5. The contoured frequency of hydrometeor water content for (from left to right) cloud ice, snow, rain, and cloud water. Contour lines are logarithmically spaced. (top) MJO wet phase. (bottom) MJO dry phase.

Another way to derive CTH and PTH was devised by *Stephens and Wood [2007]*, who defined two echo-top heights with different dBZ thresholds applied to 94-GHz radar reflectivity. Following these studies, joint histograms of CTH and PTH are constructed individually from TRMM and CloudSat observations as well as the corresponding parameters synthesized from the NICAM. The definitions of PTH and CTH in the present study are summarized in Table 1.

[22] Figures 6a and 6b indicate that the MJO wet phase well contrasts with the dry phase in the TRMM CTH-PTH histogram. The wet phase is characterized by cold cloud tops (or high CTHs) with high PR echo tops, while shallow cumulus dominates in the dry phase. It is noted that the conspicuous vertical ridge at the freezing level is due to the jump in back-scattering coefficient associated with hydrometeor melting. The CloudSat CPR histogram (Figures 6c and 6d) shows prevailing high clouds near the tropopause, whereas an increase in shallow cloud population from the wet phase to the dry phase is also evident. A majority of histogram peaks fall in the upper triangle away from the diagonal line, indicative of a significant gap between CTH and PTH, particularly where PTH is higher than the freezing

level. The portions with CTH>PTH can be attributed either to the absence of large ice particles detectable by the PR (CPR) above the 19-dBZ (10-dBZ) threshold [*Masunaga et al., 2005*] or midlevel clouds such as cumulus congestus overlapped with cirrus clouds [*Stephens and Wood, 2007*].

[23] In the synthesized 14-GHz histogram from the NICAM experiment (Figures 6e and 6f), the TRMM observation is reasonably reproduced except for the overproduction of very high PTHs (10 km or higher), which is readily expected from Figures 2 and 3. Given the abundance of snow in simulated deep convective clouds, it is seemingly

Table 1. Definitions of Cloud Top Height and Precipitation Top Height^a

	CTH	PTH
TRMM	10.8- μ m brightness temperature	19-dBZ echo-top height
CloudSat	-28-dBZ echo-top height	10-dBZ echo-top height

^aCTH, cloud top height; PTH, precipitation top height. The definition of echo-top height requires three consecutive layers with reflectivities higher than a given threshold (except for the TRMM CTH).

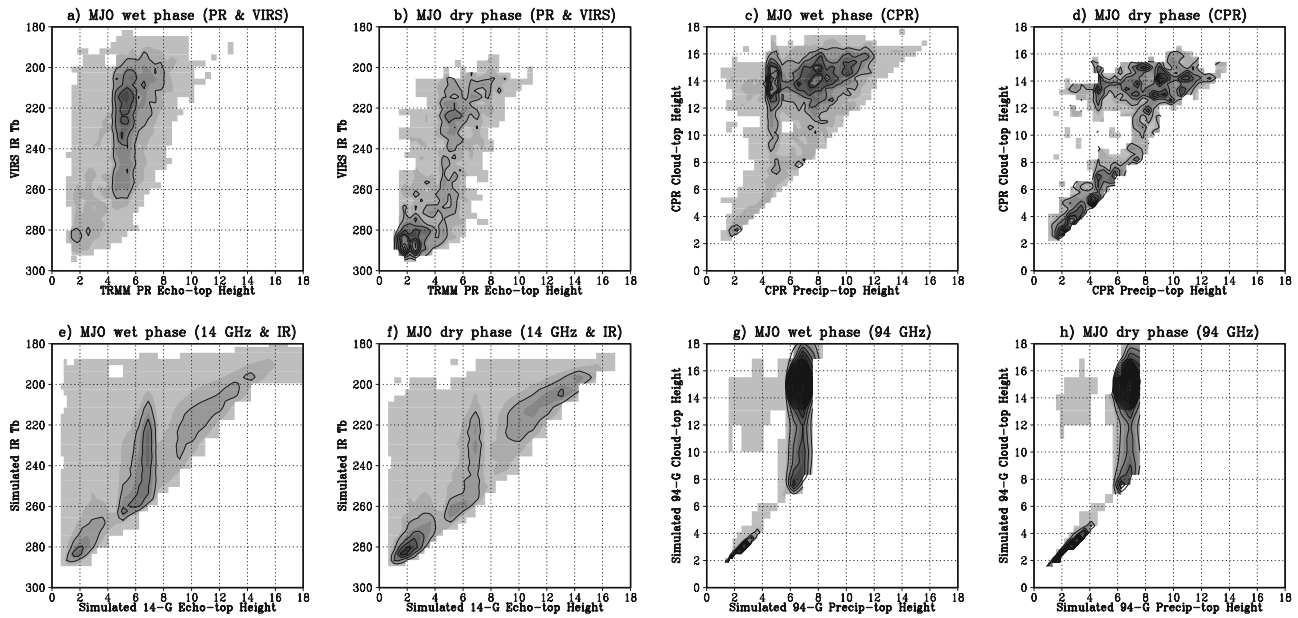


Figure 6. Joint histograms of precipitation top height (PTH, abscissa) and cloud top height (CTH, ordinate): (a) TRMM PR and VIRS histogram for the MJO wet phase. (b) Same as Figure 6a but for the MJO dry phase. (c) Same as Figure 6a but CloudSat CPR histogram. (d) Same as Figure 6b but CloudSat CPR histogram. (e–h) Same as Figures 6a–6d but synthesized from the NICAM simulation. The histograms are shaded and contoured in linear spacing.

puzzling that the domain with PTHs higher than 8 km is totally blanked out in the synthesized 94-GHz histogram (Figures 6g and 6h). This is indeed not surprising if one recalls that 94-GHz echoes higher than 5 dBZ are missing above 8 km in the NICAM simulation (Figure 4). The question to be asked is therefore narrowed down to why NICAM-simulated snow does not yield 95-GHz reflectivities higher than 5 dBZ. This problem will be addressed in section 4 below.

4. Discussion

[24] Discrepancies between actual and synthesized radar measurements can result from a variety of reasons that

involve both dynamical and microphysical factors. Radar reflectivity depends not only on hydrometeor water content but on particle size distribution (PSD). The sensitivity to particle size is very high in the Rayleigh scattering regime, where back-scattering coefficient, σ_b , increases with the 6th power of particle size. In reality, the frequency of 94 GHz, or 3.2 mm in wavelength, is comparable to the size of large snowflakes, so that the premise for the Rayleigh approximation breaks down. The sensitivity of back-scattering coefficient to particle size declines as the Rayleigh scattering regime ($\sigma_b \propto$ the 6th moment of PSD) gives way ultimately to the geometrical optics limit ($\sigma_b \propto$ the 2nd moment). The rate of increase in 94-GHz radar reflectivity

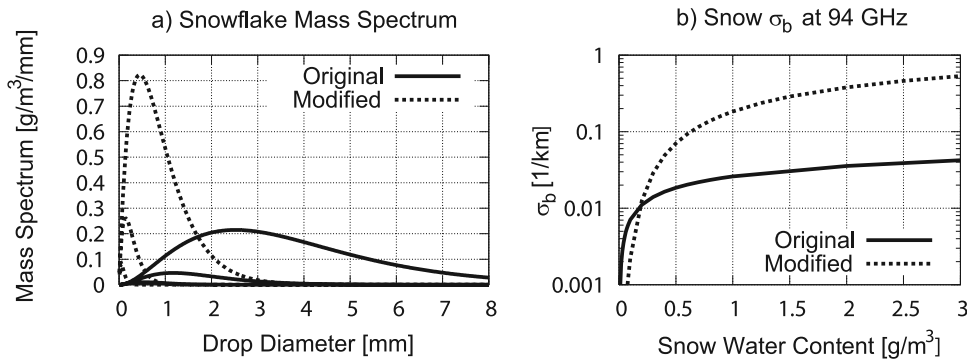


Figure 7. The original and modified particle size distributions (PSDs) of snow assumed in radar reflectivity synthesis. (a) Snow mass spectrum (or mass-weighted PSD) for the original Grabowski parameterization (solid line) and modified microphysics (dotted line). Snow water contents of 0.01, 0.1, and 1 g/m^3 are given for three curves from bottom to top. See text for details on the modification. (b) Snow back-scattering coefficient at 94 GHz as a function of snow water content for the original and modified microphysics.

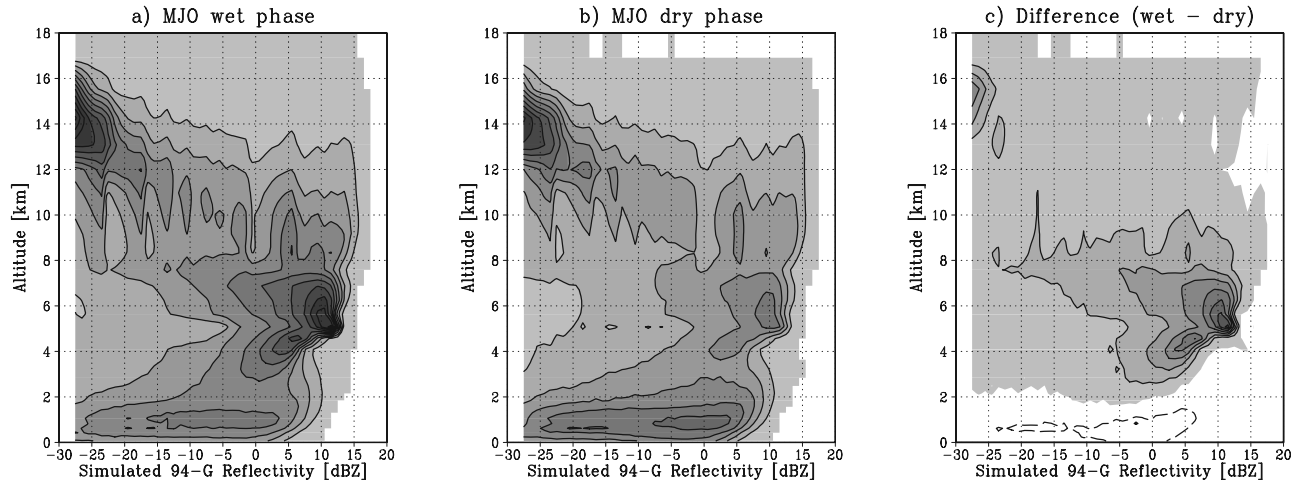


Figure 8. Same as Figures (a) 4d, (b) 4e, and (c) 4f but for the modified snow mass spectrum.

for increasing snow water content therefore tapers off when an appreciable amount of millimeter-size snowflakes are present.

[25] Figure 7a shows the snow mass spectrum for different water contents (solid lines). For the largest water content depicted (1 g/m^3), a substantial fraction of snowflakes have particle diameters larger than the 3.2-mm wavelength of CPR echo. Accordingly, the back-scattering coefficient at 94 GHz is highly insensitive to snow water content for a wide range from ~ 0.5 to 3 g/m^3 (Figure 7b). It is speculated that this nonlinearity may be a cause for the sharp cutoff in the synthesized 94-GHz CFAD (Figures 4d–4f). (Note that σ_b is drawn in logarithmic scale in Figure 7b so as to be proportional to radar reflectivity in dBZ.)

[26] The impact of the non-Rayleigh effect on radar echo is examined through a quick comparison with an additional dBZ synthesis based on modified snow microphysics. In the original *Grabowski* [1998] parameterization, the mass of a snowflake, m [kg], having the diameter, D [m], is assumed to be

$$m(D) = aD^b, \quad (1)$$

where $a = 2.5 \times 10^{-2}$ and $b = 2$. A modified snow mass spectrum is defined as $a = 5 \times 10^{-4}$ and $b = 1$ with the particle size distribution, $N(D)$, same as the original. The resultant change to the snow mass spectrum, $m(D)N(D)$, and back-scattering coefficient is shown by dotted line in Figure 7. Large snowflakes that were present in the original microphysics are replaced by many small snowflakes in the modified mass spectrum. Little fraction of snow has diameters larger than 3 mm even for a snow water content as large as 1 g/m^3 . Figure 7b shows that the modified σ_b decreases (increases) from the original σ_b for a given snow water content smaller (larger) than $\sim 0.2 \text{ g/m}^3$. This turnover in σ_b as a function of snow water content may be explained as follows. Below the turnover point, the original and modified mass spectra both lie in the Rayleigh scattering regime. Once the original mass spectrum expands beyond the Rayleigh scattering regime, however, the original σ_b starts losing the sensitivity to particle size while

the modified σ_b stays in the Rayleigh regime. As a result, the modified mass spectrum, constituted of abundant small snowflakes, is capable of producing a larger σ_b than the original mass spectrum, which consists of large but fewer snowflakes, when compared for a fixed snow water content.

[27] Figure 8 illustrates the 94-GHz CFAD synthesized from the same NICAM output as in Figures 4d–4f but using the modified snow mass spectrum. The 5-dBZ cutoff above 8 km in Figure 4 is smeared out in Figure 8, supporting the hypothesis that the non-Rayleigh effect is responsible for the problem. Correspondingly, the domain with PTHs > 8 km in the synthesized 94-GHz histogram which was found blank (Figures 6g and 6h) now contains the full of signals (Figures 9c and 9d). For the 14-GHz histogram, in contrast, the modification to snow microphysics does not increase the frequency of occurrence above 8 km but even reduces it (compare Figures 9a and 9b with Figures 6e and 6f). This does not contradict the theoretical expectation, given that neither the original nor modified microphysics suffers from the non-Rayleigh effect at the frequency of 14 GHz.

[28] Overall, reformulating the snow mass spectrum with an enhanced proportion of small snowflakes is successful in mitigating the disagreement between the simulation and observations. The modified mass spectrum, however, is still far from the best tuned microphysical model. The arc-like structure present in the original 94-GHz CFAD is destroyed by the modification at the expense of the elimination of the artificial dBZ cutoff. Some optimization technique must be developed for obtaining a desirable level of consistency with the observation. Moreover, some key processes are ignored in the present work. The modified dBZ synthesis shown in Figures 8 and 9 does not include the impact on cloud dynamics resulting from the imposed microphysical change. Although it is beyond the scope of this paper to carry out an additional NICAM experiment with modified microphysics, the expected outcome is worth speculating. The result above indicates that the current microphysical model is parameterized to assign an excessive amount of large snowflakes to a given snow water content. This deficiency could be mitigated by updating the microphysical

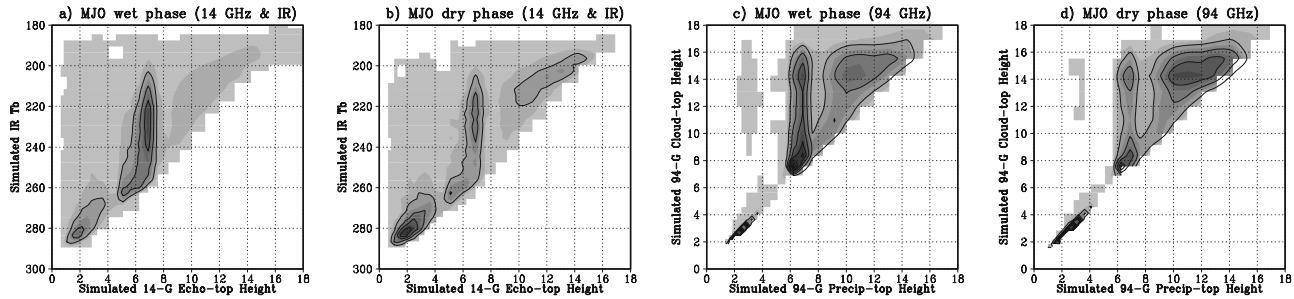


Figure 9. Same as Figures (a) 6e, (b) 6f, (c) 6g, and (d) 6h but for the modified snow mass spectrum.

scheme in some different manners. For instance, changing the coefficients a and/or b in equation (1) as done in the present paper is a simple way to adjust the snowflake size. The smaller snowflakes are, the longer they would stay aloft as the result of a reduced precipitation rate. Snowflakes thus could be advected further away before eventually precipitating out. As such, snow would be diffused over a broad area beyond where formed. This is a favorable change, since we have seen that a main issue of the current NICAM simulation is the overproduction of snow. Another possible solution is to introduce graupel, which is absent in the *Grabowski* [1998] parameterization, into the microphysical model. Graupel is less susceptible to the non-Rayleigh effect than snow since graupel has a higher particle density and is therefore smaller in mean particle size for a given mixing ratio.

[29] No microphysical scheme other than the *Grabowski* [1998] parameterization has been installed for the 2006/2007 MJO experiment studied here. On the other hand, new microphysical schemes are being developed for the NICAM and were tested for their performance by *Tomita* [2008]. *Tomita* [2008] found that the amount of ice condensate significantly decreases when graupel is included because graupel precipitates out more quickly than snow. A very recent NICAM experiment to simulate a boreal summer MJO event was performed with both the *Grabowski* [1998] microphysical model and an updated scheme with graupel included (K. Oouchi, private communication, 2008). While changes to the microphysical scheme effect the structure of individual clouds, the eastward migration of a large-scale envelope of convective clouds was successfully simulated with the NICAM regardless of microphysical schemes implemented.

[30] Radiative transfer calculations for the dBZ synthesis rely on the Mie approximation, where hydrometeors are assumed to be spherical. The Mie approximation is justifiable for liquid particles, whereas ice crystals and snowflakes are highly anisotropic in shape. Equation (1) not only controls the hydrometeor mass spectrum but also regulates the particle morphology depending on the parameter b . A snowflake may be considered to be two dimensional (plate-like) for $b = 2$ and one dimensional (needlelike) for $b = 1$. Our radiative transfer scheme is currently not designed to account for the morphologic effect on the back-scattering and extinction coefficients. In reality, frozen hydrometeors are so complicated in crystal structure that the exact modeling of their radiative properties is practically impossible. A simplified but reasonably realistic parameterization

of the radiative properties will be required for a better treatment of cloud ice and snow in the dBZ synthesis.

5. Conclusions

[31] Cloud and precipitation properties simulated by a GCRM are analyzed jointly with satellite measurements. The GCRM simulation used in this study is provided by the NICAM. The study period is the 32-day sequence starting from 15 December 2006, which contains a major portion of an Madden-Julian Oscillation event. Radiative transfer calculations are applied to the NICAM output to synthesize virtual observations for comparison with TRMM and CloudSat measurements. Analysis with the composite diagram supports the conclusion of *Miura et al.* [2007] that the GCRM reproduces a slow, eastward migration of a convective envelope well comparable to the satellite measurement. CFADs are constructed separately for the wet and dry phases of the MJO, which are isolated out by bandpass filtering. In the TRMM PR CFAD, a contrast between the wet and dry phases is clearly marked by the predominance of deep (shallow) precipitation in the wet (dry) phase. The CloudSat CPR CFAD confirms this contrast but also indicates the prevalence of cirrus clouds independently of the MJO phases. The GCRM CFAD qualitatively reproduces the TRMM and CloudSat CFADs, except that the GCRM tends to overly produce snow in deep convection particularly in the MJO dry phase. The joint histograms of cloud top and precipitation top are created individually from TRMM and CloudSat measurements. The synthesized TRMM histogram again indicates that snow is excessively produced in simulated deep convective clouds, while the synthesized 94-GHz histogram lacks radar echoes above 8 km in altitude. The latter is found to arise from the non-Rayleigh scattering effect that the 94-GHz back-scattering coefficient loses the sensitivity to an increase in snow water content when mean particle size is comparable to the wavelength of radar echo. A modification to microphysical parameterization by redefining the snow mass spectrum with an enhanced proportion of smaller particles turns out to offset the model bias.

[32] The current paper is not intended to provide the complete list of remedies against the deficiencies inherent in the particular model. Instead, this work is aimed at sketching out a general methodology to diagnose the simulated cloud and precipitation properties in comparison with satellite measurements. The methodology is directly applicable to a variety of cloud models including the MMF as well as GCRM. T. Matsui et al. (Evaluation of long-term cloud-

resolving model simulations using satellite radiance observations and multi-frequency satellite simulators, submitted to *Journal of Atmospheric and Oceanic Technology*, (2008) demonstrates a recent effort to assess the performance of their CRM on the basis of a similar analysis technique to the present method. An intriguing implication of the present findings is that combined use of the TRMM PR and CloudSat CPR has the potential to evaluate not only macrophysical variables such as snow water content but the microphysical parameterizations of cloud models.

[33] **Acknowledgments.** The authors acknowledge the work of the NICAM development group, NASA CloudSat project, and the NASA and JAXA TRMM project teams. The data used in this work were made available by their dedicated efforts. This study is partly supported by the Virtual Laboratory for the Earth's Climate Diagnostics.

References

- Berg, W., T. S. L'Ecuyer, and C. D. Kummerow (2006), Rainfall climate regimes: The relationship of regional TRMM rainfall biases to the environment, *J. Appl. Meteor. Climatol.*, *45*, 434–454.
- Grabowski, W. W. (1998), Toward cloud resolving modeling of large-scale tropical circulations: A simple cloud microphysics parameterization, *J. Atmos. Sci.*, *55*, 3283–3298.
- Grabowski, W. W. (2003), MJO-like coherent structures: Sensitivity simulations using the cloud-resolving convection parameterization (CRCP), *J. Atmos. Sci.*, *60*, 847–864.
- Heymsfield, A. J., and C. M. R. Platt (1984), A parameterization of the particle size spectrum of ice clouds in terms of the ambient temperature and the ice water content, *J. Atmos. Sci.*, *41*, 846–855.
- Inoue, T., M. Satoh, H. Miura, and B. Mapes (2008), Characteristics of cloud size of deep convection simulated by a global cloud resolving model over the western tropical Pacific, *J. Meteorol. Soc. Jpn.*, in press.
- Kiladis, G. N., K. H. Straub, and P. T. Haertel (2005), Zonal and vertical structure of the Madden-Julian Oscillation, *J. Atmos. Sci.*, *62*, 2790–2809.
- Lin, J. L., et al. (2006), Tropical intraseasonal variability in 14 IPCC AR4 climate models. Part I: Convective signals, *J. Clim.*, *19*, 2665–2690.
- Lin, X., and R. H. Johnson (1996), Kinematic and thermodynamic characteristics of the flow over the western Pacific warm pool during TOGA COARE, *J. Atmos. Sci.*, *53*, 695–715.
- Madden, R. A., and P. R. Julian (1971), Detection of a 40–50 day oscillation in the zonal wind in the tropical Pacific, *J. Atmos. Sci.*, *28*, 702–708.
- Madden, R. A., and P. R. Julian (1972), Description of global-scale circulation cells in the tropics with a 40–50 day period, *J. Atmos. Sci.*, *29*, 1109–1123.
- Masunaga, H., and C. D. Kummerow (2005), Combined radar and radio-meter analysis of precipitation profiles for a parametric retrieval algorithm, *J. Atmos. Oceanic Technol.*, *22*, 909–929.
- Masunaga, H., and C. D. Kummerow (2006), Observations of tropical precipitating clouds ranging from shallow to deep convective systems, *Geophys. Res. Lett.*, *33*, L16805, doi:10.1029/2006GL026547.
- Masunaga, H., T. Iguchi, R. Oki, and M. Kachi (2002), Comparison of rainfall products derived from TRMM Microwave Imager and Precipitation Radar, *J. Appl. Meteorol.*, *41*, 849–862.
- Masunaga, H., T. S. L'Ecuyer, and C. D. Kummerow (2005), Variability in the characteristics of precipitation systems in the tropical Pacific. Part I: Spatial structure, *J. Clim.*, *18*, 823–840.
- Masunaga, H., T. S. L'Ecuyer, and C. D. Kummerow (2006), The Madden-Julian Oscillation recorded in early observations from the Tropical Rainfall Measuring Mission (TRMM), *J. Atmos. Sci.*, *63*, 2777–2794.
- Miura, H., M. Satoh, T. Nasuno, A. T. Noda, and K. Oouchi (2007), A Madden-Julian Oscillation event realistically simulated by a global cloud-resolving model, *Science*, *318*, 1763–1765, doi:10.1126/science.1148443.
- Morita, J., Y. N. Takayabu, S. Shige, and Y. Kodama (2006), Analysis of rainfall characteristics of the Madden-Julian Oscillation using TRMM satellite data, *Dyn. Atmos. Oceans*, *42*, 107–126.
- Nakazawa, T. (1988), Tropical super clusters within intraseasonal variations over the western Pacific, *J. Meteorol. Soc. Jpn.*, *66*, 823–839.
- Nasuno, T., H. Tomita, S. Iga, H. Miura, and M. Satoh (2008), Convectively coupled equatorial waves simulated by a global nonhydrostatic experiment on an aqua planet, *J. Atmos. Sci.*, *65*, 1246–1265.
- Olson, W. W., P. Bauer, N. F. Viltard, D. E. Johnson, W.-K. Tao, R. Meneghini, and L. Liao (2001), A melting-layer model for passive/active microwave remote sensing applications. Part I: Model formulation and comparison with observations, *J. Appl. Meteorol.*, *40*, 1145–1163.
- Randall, D., M. Khairoutdinov, A. Arakawa, and W. Grabowski (2003), Breaking the cloud parameterization deadlock, *Bull. Am. Meteorol. Soc.*, *84*, 1547–1564.
- Satoh, M., T. Matsuno, H. Tomita, H. Miura, T. Nasuno, and S. Iga (2008a), Nonhydrostatic icosahedral atmospheric model (NICAM) for global cloud resolving simulations, *J. Comput. Phys.*, *227*, 3486–3514.
- Satoh, M., T. Nasuno, H. Miura, H. Tomita, S. Iga, and Y. Takayabu (2008b), Precipitation statistics comparison between global cloud resolving simulation with NICAM and TRMM PR data, in *High Resolution Numerical Modelling of the Atmosphere and Ocean*, edited by K. Hamilton and W. Ohfuchi, pp. 99–112, Springer, New York.
- Slingo, J. M., et al. (1996), Intraseasonal oscillations in 15 atmospheric general circulation models: results from an AMIP diagnostic subproject, *Clim. Dyn.*, *12*, 325–357.
- Stephens, G. L., and N. B. Wood (2007), Properties of tropical convection observed by millimeter-wave radar systems, *Mon. Weather Rev.*, *135*, 821–842.
- Tomita, H. (2008), New microphysics with five and six categories with diagnostic generation of cloud ice, *J. Meteorol. Soc. Jpn.*, in press..
- Tomita, H., H. Miura, S. Iga, T. Nasuno, and M. Satoh (2005), A global cloud-resolving simulation: Preliminary results from an aqua planet experiment, *Geophys. Res. Lett.*, *32*, L08805, doi:10.1029/2005GL022459.
- Yang, G.-Y., and J. Slingo (2001), The diurnal cycle in the tropics, *Mon. Weather Rev.*, *129*, 784–801.

H. Masunaga, Hydrospheric Atmospheric Research Center, Nagoya University, F3-1(200) Furocho Chikusa-ku, Nagoya 464-8601, Japan. (masunaga@hyarc.nagoya-u.ac.jp)

H. Miura, Frontier Research Center for Global Change, Japan Agency for Marine-Earth Science and Technology, 3173-25 Showamachi, Kanazawa-ku, Yokohama, Kanagawa 236-0001, Japan. (miurah@jamstec.go.jp)

M. Satoh, Center for Climate System Research, University of Tokyo, 5-1-5 Kashiwanoha, Kashiwa, Tokyo, Chiba 277-8568, Japan. (satoh@ccsr.u-tokyo.ac.jp)